Journal of Materials Research and Technology 33 (2024) 5909–5921

Contents lists available at ScienceDirect

Journal of Materials Research and Technology

journal homepage: www.elsevier.com/locate/jmrt

Jaya algorithm hybridized with extreme gradient boosting to predict the corrosion-induced mass loss of agro-waste based monolithic and Ni-reinforced porous alumina

T.T. Dele-Afolabi [a,b,*], D.W. Jung [c,**], Masoud Ahmadipour [a,d], M.A. Azmah Hanim [e,f], A.O. Adeleke [g], M. Kandasamy [h,i], Prem Gunnasegaran [a]

[a] Institute of Power Engineering, Universiti Tenaga Nasional, Jalan Ikram UNITEN, 43000, Kajang, Selangor, Malaysia
[b] Department of Mechanical Engineering, Faculty of Engineering, Ajayi Crowther University, P.M.B. 1066, Oyo, Oyo State, Nigeria
[c] Department of Mechanical Engineering, Jeju National University, 1 Ara 1-dong, Jeju, 690-756, South Korea
[d] School of Electrical Engineering, College of Engineering, Universiti Teknologi MARA, 40450, Shah Alam, Selangor, Malaysia
[e] Department of Mechanical and Manufacturing Engineering, Faculty of Engineering, Universiti Putra Malaysia, 43400, UPM Serdang Selangor, Malaysia
[f] Advance Engineering Materials and Composites Research Center, (AEMC), Faculty of Engineering, Universiti Putra Malaysia, 43400, UPM Serdang Selangor, Malaysia
[g] Institute of Energy Infrastructure (IEI), Universiti Tenaga Nasional, Jalan Ikram UNITEN, 43000, Kajang, Selangor, Malaysia
[h] Department of Electrochemistry, Saveetha School of Engineering, SIMATS, Thandalam, Chennai, Tamil Nadu, 602105, India
[i] Department of Chemistry, K.Ramakrishnan College of Technology, Samayapuram, Tiruchirappalli, 621 112, Tamil Nadu, India

ARTICLE INFO

Handling editor: P.Y. Chen

Keywords:
Porous alumina
Composites
Corrosion resistance
Agro-waste PFAs
Extreme gradient boosting
Jaya algorithm

ABSTRACT

Chemical attack is one of the most significant issues affecting porous ceramic systems employed as membranes for separation technologies, which necessitate frequent system reliability testing. In this work, the non-linear predictive power of a hybridized machine learning prediction model, specifically Jaya-XGBoost to predict the corrosion-induced mass loss of monolithic and nickel-reinforced porous alumina ceramics has been examined. This study demonstrates the mass loss of monolithic and Ni-reinforced porous alumina developed using rice husk and sugarcane bagasse in acidic and alkaline corrosive media. Based on empirical findings, the formation of a very stable $Ni_3Al_2SiO_8$ spinelloid phase in the RH-graded composites increased their chemical stability in the corrosive environments compared to their monolithic and corresponding SCB-graded counterparts. Corrosion testing data of these specimens were collected and fitted into both XGBoost and Jaya-XGBoost machine learning algorithms. The results showed that the Jaya-XGBoost model performed better in predicting the corrosion-induced mass loss of both the monolithic and the nickel-reinforced porous alumina than the regular XGBoost model in terms of statistical accuracy measures. The Jaya-XGBoost model developed in this study effectively predicted the mass loss in NaOH ($R^2 = 0.9984$; MAE = 0.0168) and mass loss in H_2SO_4 ($R^2 = 0.9824$; MAE = 0.0217) of the monolithic and nickel-reinforced porous alumina. The precision that can be obtained by modifying hyper-parameters with the Jaya method, combined with the well-known accuracy of XGBoost, renders the proposed model novel.

1. Introduction

The rapidly growing field of membrane technology for wastewater treatment and solid separation has recently attracted the attention of industry experts and researchers seeking to fabricate porous materials with the properties required to perform well under these demanding operating environments [1–8]. In contrast to alternative porous materials, alumina has been thoroughly researched as a viable ceramic for the manufacturing of porous systems owing to its remarkable inherent qualities and affordable price [9–14]. Nevertheless, the intrinsic brittleness and sensitivity to post-fabrication procedures of porous alumina materials, like those of other ceramics, have limited their potential as a good fit for a variety of load-bearing and harsh operating conditions [15,16]. In order to give the best microstructural

* Corresponding author. Institute of Power Engineering, Universiti Tenaga Nasional, Jalan Ikram UNITEN, 43000, Kajang, Selangor, Malaysia.
** Corresponding author.
E-mail addresses: temitope@uniten.edu.my (T.T. Dele-Afolabi), jungdw77@naver.com (D.W. Jung).

https://doi.org/10.1016/j.jmrt.2024.10.221
Received 21 August 2024; Received in revised form 15 October 2024; Accepted 26 October 2024
Available online 28 October 2024

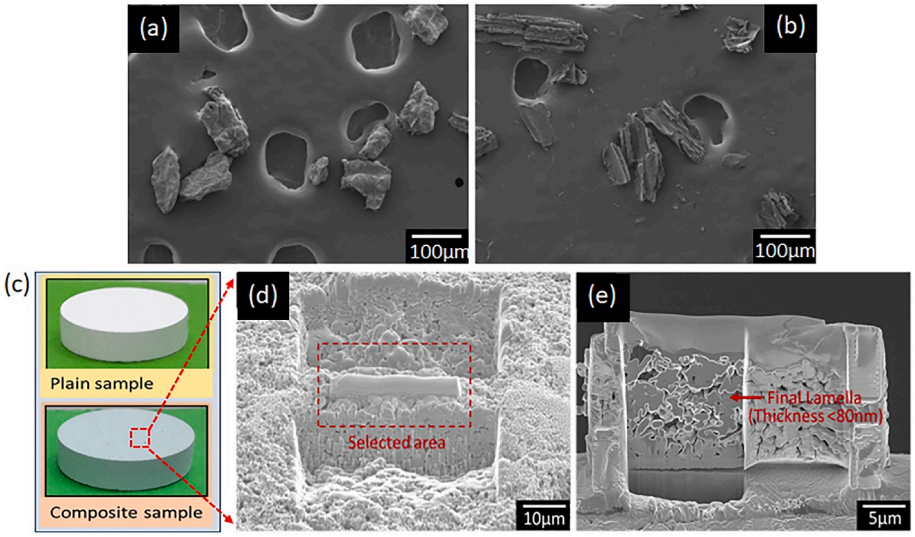

Fig. 1. FESEM microstructures of (a) rice husk (RH), and (b) sugarcane bagasse (SCB) pore formers; (c) the developed porous ceramic samples, (d,e) preparation of TEM sample from a selected spot and sample thinning on Cu grid.

resilience in extremely corrosive discharges related to any of the aforementioned separation processes, new porous materials with excellent characteristics are required.

The remarkable mechanical and corrosion-resistant properties of nickel have made it a popular choice for enhancing the durability of ceramic materials [17–20]. Nickel offers microstructural refinement and chemical stability, making it a promising reinforcing element for alumina. These benefits come from spinel being created in-situ by a chemical reaction between nickel and alumina under high pressure and temperature. Numerous studies have reported on the enhancement of pore-matrix constituents in the $NiAl_2O_4/Al_2O_3$ membrane composites produced by the in-situ reaction between nickel (II) oxide and alumina [21,22]. $NiAl_2O_4/Al_2O_3$ membrane composites have been the subject of numerous investigations that have shown the improvement of pore-matrix components. Given this, earlier studies [23–25] have demonstrated that the nickel aluminate spinel structure ($NiAl_2O_4$) displays a high level of resilience when subjected to severe acid and alkali attacks.

With a view to advancing the campaign for 'zero waste' [26,27], especially in developing nations that have not yet discovered permanent remedies for global environmental issues, a number of agricultural waste materials have been sought in developing porous ceramic systems through the pore-forming agent processing technique [28–30]. Their ability to function as a complimentary silica (SiO_2) source and a pore former in the resulting porous ceramics has led to the rise in prominence of agro-waste pore-forming agents. In light of this, it is thought that agricultural wastes can be used as effective pore-forming materials to modify the intrinsic properties of porous ceramics [31,32]. This is because of the different capacities that these materials have for retaining SiO_2 residue after thermal degradation. Selecting agro-waste PFA can be a helpful processing parameter for enhancing the resistance of porous ceramic materials to chemical attack, as we discovered in our earlier study [33]. This offers information on the optimal operating conditions that ensure the materials will perform to their maximum potential.

Predictive models for porous ceramics and associated fields have been developed in recent times using precise and reliable computational intelligence, such as neural networks (ANN) [34,35], random forests (RF) [36,37], adaptive neuro-fuzzy inference system (ANFIS) [38,39], and gaussian process regression (GPR) [40]. An ANN model was utilized in our previous study [35] to predict the corrosion-induced mass loss of porous Al_2O_3/Ni composites. Unfortunately, the model's statistical evaluation criteria suggested that the prediction accuracy may be improved, in contrast to prior studies [41,42] that revealed ANN's instability as a predictor. Artificial neural networks are impaired by concerns of algorithm parameter alteration, over-fitting, inefficient training, and inefficient testing. Therefore, for the purpose of improving the generalization and robustness of prediction models, it is essential to investigate alternative highly effective machine learning algorithm methods.

One of the most advanced algorithms based on Friedman's gradient boosting decision [43] is the extreme gradient boosting (XGBoost) algorithm developed by Chen and Guestrin [44]. Natural selection and successful use of the algorithm for regression problems in a wide range of scientific and technological disciplines can be attributed to its significant flexibility and versatility, which enable it to provide greater performance and accuracy than other algorithms. Through correlation analysis between physical parameters like porosity and corrosion resistance behavior, the XGBoost model can provide new insights into determining the durability of porous ceramics and aid in the optimization of material composition for use in specific environments. Nevertheless, choosing the XGBoost hyperparameters, which have a huge impact on the prediction outcomes, is very difficult. Previous studies suggest that an efficient heuristic approach can overcome this constraint [45,46].

Inspired by the popularity and potential applications of the TLBO (teaching–learning based optimization) method, Rao [47] introduced the parameter-less Jaya algorithm to solve both constrained and unconstrained optimization problems. The Jaya algorithm is unique in that it relies only on two parameters: the number of iterations and the size of the population. This algorithm's attractiveness lies in its ability to lower the worst solution in the same iteration while still providing the ideal solution. Abhishek et al. [48] demonstrated the computational simplicity and reliable prediction outcome of fuzzy inference system (FIS) integrated with Jaya optimization algorithm in selecting the optimal process parameters during the machining of carbon fibre-reinforced epoxy composites. The artificial neural network (ANN) model optimized using the Jaya algorithm demonstrated superior convergence and a very acceptable error rate in predicting the mechanical properties of glass fibre-reinforced composites when compared to particle swarm optimization (PSO), as demonstrated by Fahem et al. [49].

While some attempts have been made to analyze porous ceramic systems using machine learning techniques, most of the research that have already been done are based on simple models that are prone to

overfitting, algorithm tweaking, and ineffective training. With XGBoost and the optimization of the representative model by the Jaya algorithm, the current work thus aims to develop a predictive model for predicting the corrosion-induced mass loss of monolithic and nickel-reinforced porous alumina subjected to strong corrosive environments. To our knowledge, this is the first technique of using the Jaya-XGBoost model to predict the corrosion resistance performance of porous ceramic materials.

2. Experimental study

2.1. Starting materials and fabrication

In this work, the pore formers were rice husk and sugarcane bagasse, while the ceramic matrix was made of alumina and the reinforcing material was nickel. Before being introduced as pore formers, rice husk and sugarcane bagasse (Fig. 1a and b) were crushed, processed in an acidic solution and screened to get particles measuring between 63 and 125 μm in size. The alumina and pore forming powders (5, 10, and 15 wt %) for the monolithic porous alumina ceramics were manually mixed with sucrose solution for 5 min in an agate mortar after being dry milled for 1 h at 300 rpm. A slightly different strategy was applied in the instance of the Ni-reinforced porous alumina. First, the alumina and nickel powders (2, 4, 6, and 8 wt%) were wet milled in ethanol for 12 h at 550 rpm, followed by a 6-h dry milling period at the same speed. Following that, the very same process described above for the monolithic samples was applied to the pore formers (fixed at 10 wt%) and composite blend. The entire sample compositions were cold pressed at 95 MPa in a steel die. The heat treatment method for the pore former decomposition in the samples was optimized using the thermal behavior of the agro-waste PFAs. This involved a stepwise temperature increment of 1 °C/min and a 1-h dwell time at each of the following temperature ranges: 200, 300, 500, and 800 °C. Subsequently, the samples were sintered at 1450 °C for 2 h, with a heating rate of 5 °C/min. Fig. 1c shows the defect-free monolithic and Ni-reinforced porous alumina produced in this study.

2.2. Sample characterization

The ratio of density measured using the Archimedes approach to the ideal density of completely dense monolithic/composite samples was used to calculate the porosity. An X-ray diffractometer with CuKα radiation (wave length = 1.5406 Å) at 40 kV and 40 mA was used to determine the phase composition. The samples were ground, polished, and ultrasonically treated in order to examine the structure of the monolithic and Ni-reinforced porous ceramics. The pore morphology of the samples and the granular microstructure of the composite samples were both observed using field emission scanning electron microscopy (FESEM) and transmission electron microscopy (TEM), respectively. Additionally, a dual beam system's focused ion beam (FIB) and SEM were employed to provide a high-quality electron transparent sample (lamella thickness <80 nm) for the TEM investigation (Fig. 1d and e).

2.3. Corrosion resistance test

The mass loss upon heating in alkaline and acidic environments was used to characterize the chemical durability of the monolithic and Ni-reinforced porous ceramics. After being ultrasonically cleaned in ethanol and weighed, the samples were then immersed in hot aqueous solutions (110 °C) containing 10 wt% NaOH and 20 wt% H_2SO_4 (according to the Chinese standard, GB/T 1970-96) for 2, 4, 6, and 8 h. Samples were ultrasonically washed after each corrosion test to get rid of any remaining solution and loose corrosion products. After that, samples were allowed to dry to achieve a fixed mass so that the % mass loss could be calculated. For each sample composition, the test was repeated twice to guarantee the consistency of the empirical data. Finally, FESEM equipment was used to analyze the microstructures of porous ceramic samples that had corroded in strong alkaline and acidic environments.

3. Proposed models

3.1. Extreme gradient boosting (XGBoost)

Considering the microstructural degradation and strength deterioration of porous ceramic systems used as separation membrane units under extreme service conditions, XGBoost algorithm was utilized in this study for developing the prediction model for corrosion-induced mass loss of agricultural waste-based porous ceramics. XGBoost, a tree ensemble algorithm developed by Chen and Guestrin, builds upon Friedman's gradient boosting (GB) method. Its exceptional efficiency and great forecast accuracy have garnered significant attention in recent times. Its ability to produce boosted trees and operate concurrently makes it adept at handling regression and classification tasks efficiently. Similar to many optimization techniques, XGBoost's essence lies in identifying the best variables for a given objective function (OA) through machine learning methodologies, particularly gradient boosting criteria [44].

XGBoost may also simultaneously enhance trees, just like GB decision trees and GB machines. This enables it to quickly generate trustworthy models for various engineering simulations. Notably, XGBoost is distinguished by its 'regularized boosting' technology, a feature not found in traditional gradient boosting implementations. By integrating this innovative algorithm with the gradient boosting approach, XGBoost ultimately achieves improved model accuracy. The description of XGBoost is as: Let $D_1 = \{(x_i, y_i)\}$ be a dataset with n samples and m features $(|D_1| = n, x_i \epsilon R^m, y_i \epsilon R)$. The proposed tree ensemble model employs additive functions to approximate the system's response [44]:

$$\widehat{y_i} = \varphi(x_i) = \sum_{z=1}^{Z} f_z(x_i), f_z \epsilon F \tag{1}$$

where, F is the regression tree space. It is described as

$$F = \{f(x) = \omega_q(x)\}(q : R^m \to T, \omega \epsilon R^T) \tag{2}$$

in which q is the structure of trees, ω indicates e weight of the leaf, and T indicates the quantity of leaves on the tree. Meanwhile, a function that correlates to q is termed f_k, and ω correlates to an independent tree. XGBoost minimizes its objective function (OA) in order to optimize the ensemble tree and minimize error [44].

$$L^{(t)} = \sum_{i=1}^{n} l\left(y_i, \widehat{y_i^{(t-1)}} + f_t(x_i)\right) + \Omega(f_t) \tag{3}$$

$$\Omega(f_k) = \gamma T + \frac{1}{2}\lambda \|w\|^2 \tag{4}$$

in which, the difference between measured and predicted values is quantified using the convex loss function, l, $\widehat{y_i}$ is predicted value, y_i is measured value, t is number of iterations to minimize the errors, Ω is the model's complexity.

3.2. Jaya algorithm

The Jaya heuristic algorithm is a swarm intelligence-based method. It is a straightforward yet effective optimization strategy meant to handle optimization issues that are both confined and unconstrained. Unlike previous heuristic algorithms such as the Genetic Algorithm (GA), which used certain selection operators, crossover probability, and mutation probability as control parameters, the Jaya algorithm distinguishes itself by using only commonly utilized control parameters. It eliminates the need for algorithm-specific control parameters, simplifying its application and setting it apart from other heuristic techniques.

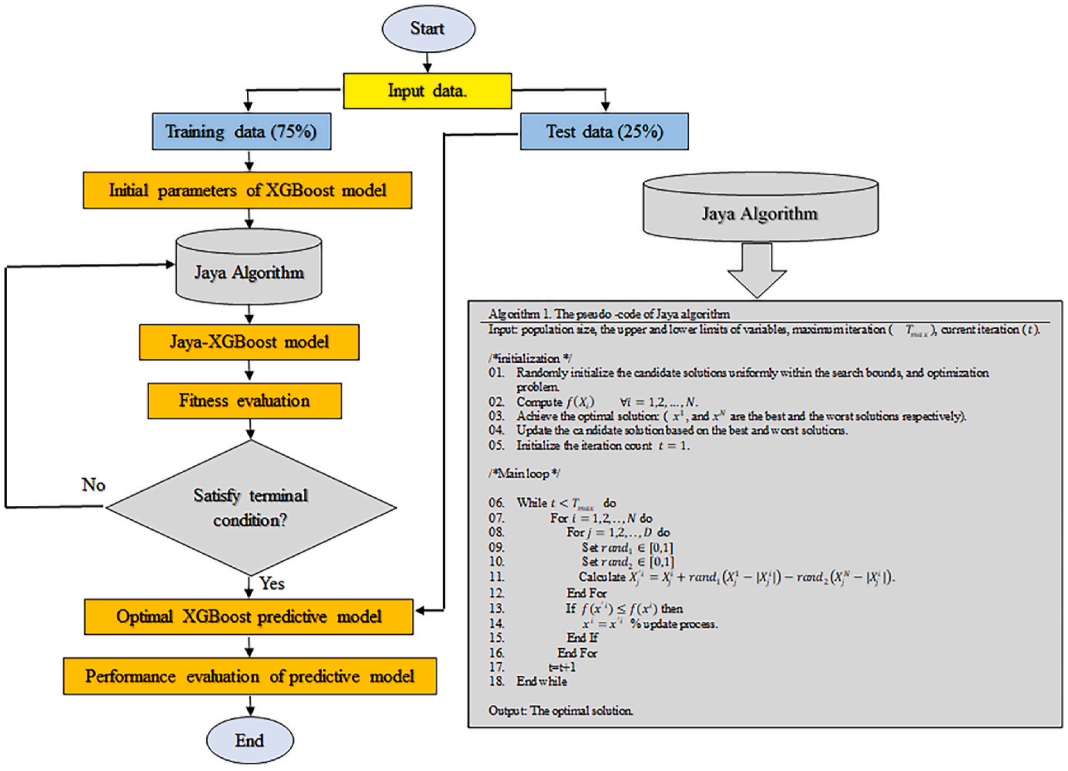

Fig. 2. The structure of Jaya-XGBoost model for prediction.

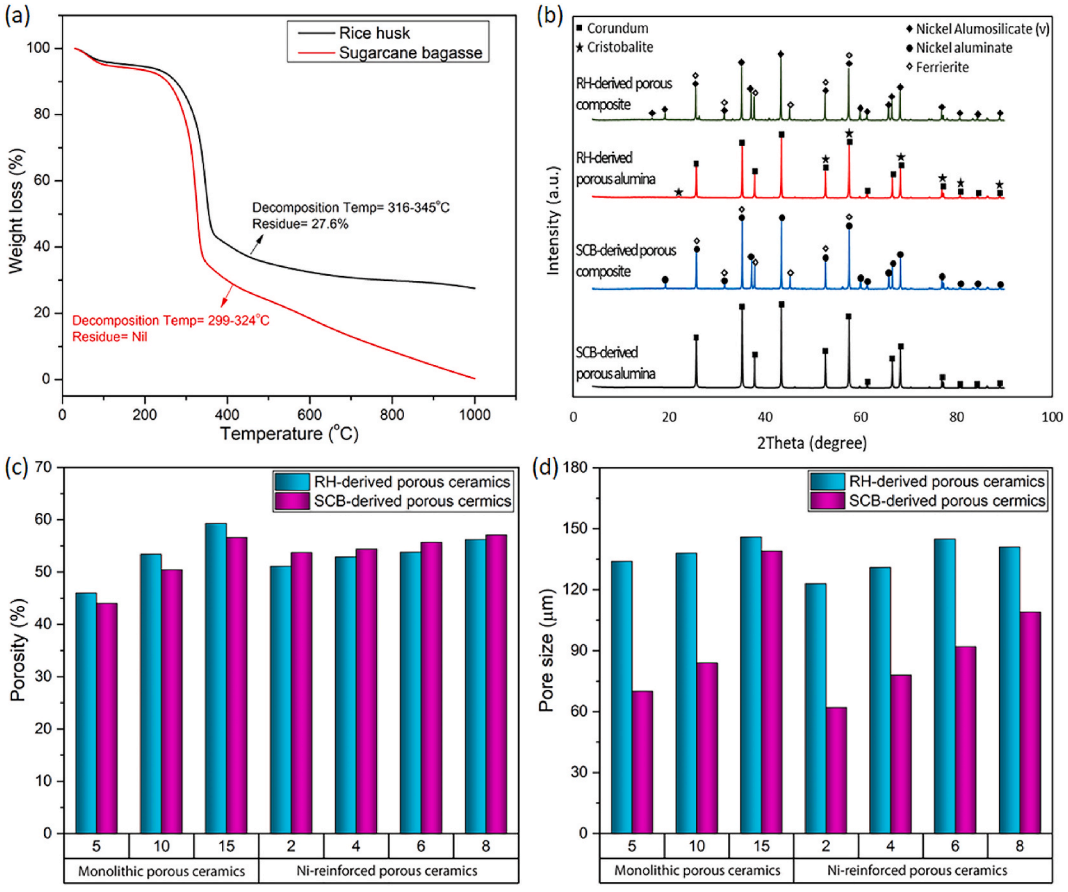

Fig. 3. (a) TGA plots for the rice husk and sugarcane bagasse, (b) XRD patterns of the different porous systems; plots of (c) porosity values, and (d) pore sizes of the RH and SCB-derived porous ceramics.

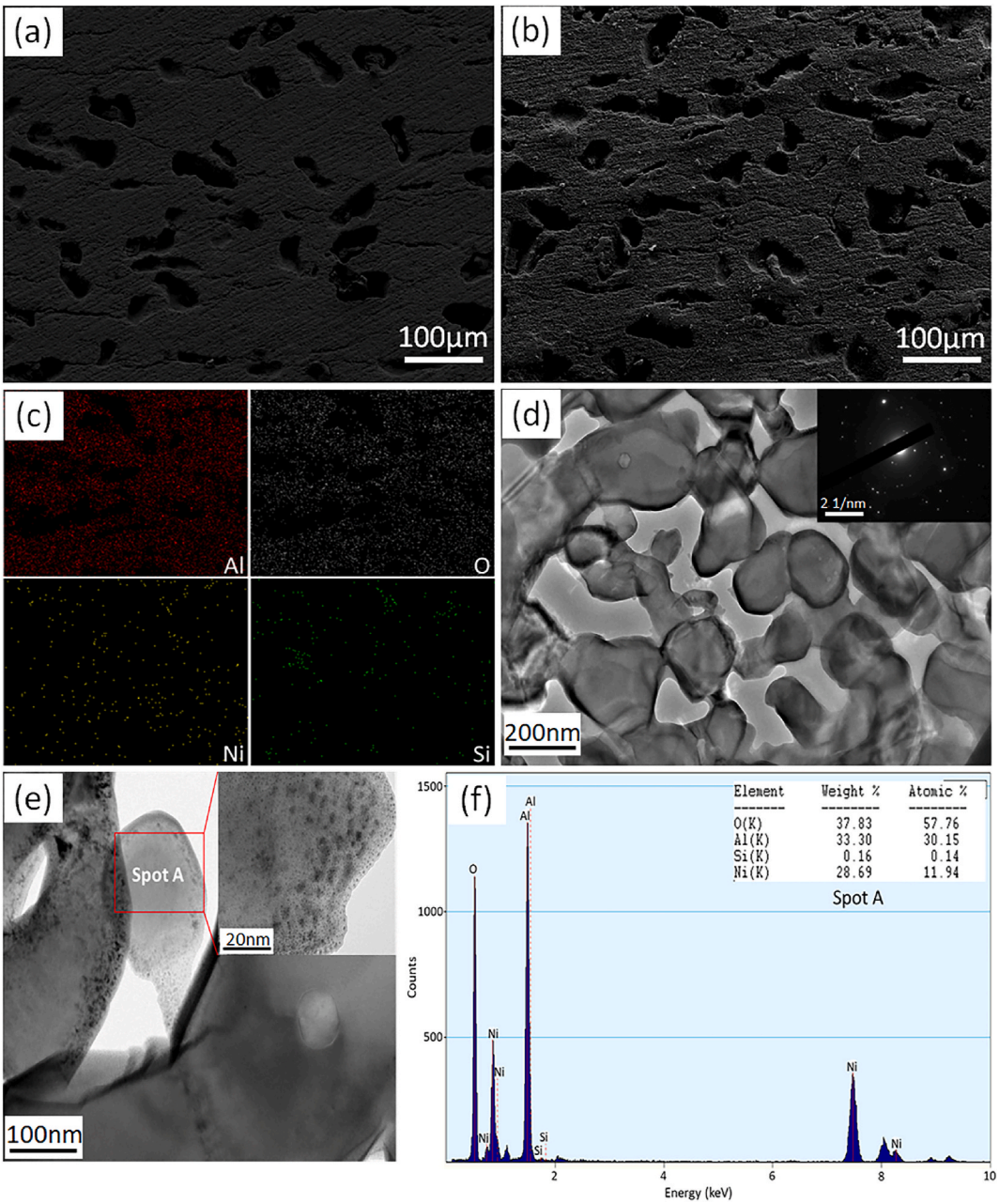

Fig. 4. FESEM images showing microstructures of RH-derived (a) monolithic porous alumina, (b) Ni-reinforced porous alumina and its corresponding (c) EDS elemental maps; (d), (e) FETEM microstructures of the RH-derived Ni-reinforced porous alumina, and (f) EDS spectrum of spot A.

The underlying principle of the Jaya algorithm is to continuously avoid the least favorable outcome within the objective function while actively pursuing the most optimal solution in each iteration. Imagine the objective function as $f(a)$. In a given iteration i, where there exist design variables ($M = 1,2,\ldots,m$) and candidate solutions ($N = 1,2,\ldots,n$), let A_{MN_i} represent the value of the $M-th$ variable of the $N-th$ candidate during the $i-th$ iteration. We can then derive the following formula [46]:

$$A'_{MN_i} = R1_{Mi}\left(A_{M\ best_i} - \left|A_{MN_i}\right| + A_{MN_i} - R2_{Mi}\left(A_{M\ \ worst\ i} - \left|A_{MN_i}\right|\right)\right) \quad (5)$$

in which, $A_{M\ best_i}$ representing the $M-$ variable value for the best candidate, $A_{M\ \ worst\ i}$ representing the $M-$ variable value for the worst candidate, and A'_{MN_i} signifying the updated value of the $M-$ variable. $R1$ and $R2$ denote two random numbers for the $M-$ variable within the range [0, 1] in the $i-th$ iteration. Whenever the formula yields a superior target value, A_{MN_i} undergoes replacement [50].

Fig. 2 illustrates the theoretical procedure and the overall study operation for the designed hybrid Jaya-XGBoost.

3.3. Evaluation criteria

This work uses a training set to train the predictive model and a test set to validate the trained model, as shown in Fig. 2. Furthermore, the quality of the models is compared and assessed using performance scores of model evaluation indices, namely the determination coefficient (R^2), the mean absolute error (MAE), and the root mean square error (RMSE), in order to evaluate the accuracy and reliability of the hybrid model in this work. These assessment indices are used to describe how the measured and predicted values of databases relate to one another. The following are the formulas for calculating these assessment indicators [51].

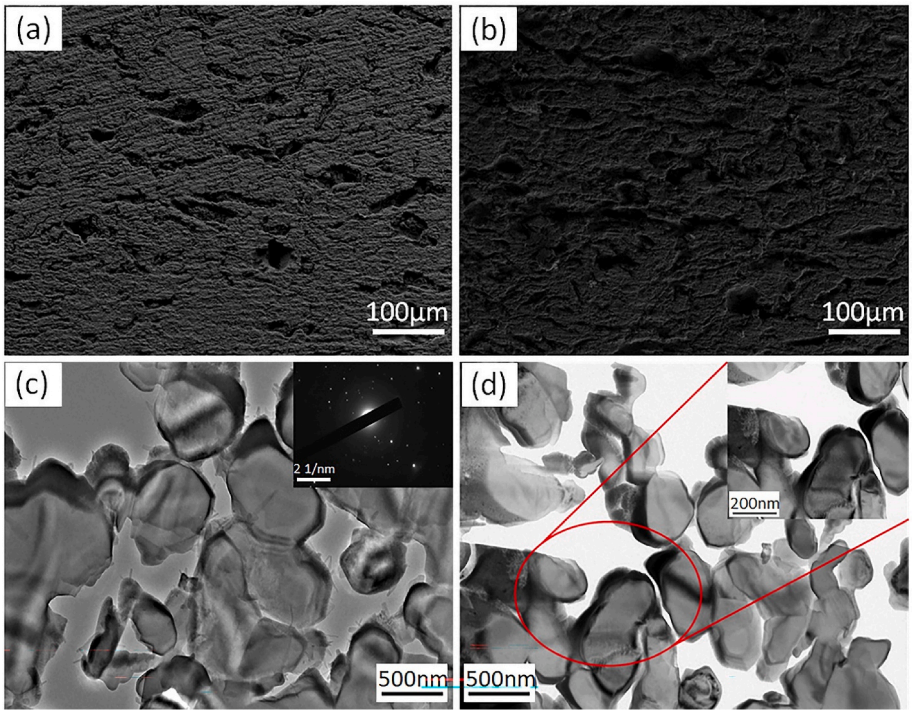

Fig. 5. FESEM images showing microstructures of SCB-derived (a) monolithic porous alumina, and (b) Ni-reinforced porous alumina; (c),(d) FETEM microstructures of the SCB-derived Ni-reinforced porous alumina.

$$RMSE = \left(\frac{1}{N}\sum_{i=1}^{N}(\widehat{y}_i - y_i)^2\right)^{1/2} \tag{6}$$

$$R^2 = \frac{1 - \sum_i (y_i - \widehat{y}_i)^2}{\sum_i (y_i - \overline{y}_i)^2} \tag{7}$$

$$MAE = \frac{1}{N}\sum_{i=1}^{N}|y_i - \widehat{y}_i| \tag{8}$$

in which y_i shows the observed database value, $\widehat{y}_i$ is the predicted database value of the model, $\overline{y}_i$ is the average of the observed database values, and N denotes the number of samples in the training or testing stages.

4. Results and discussion

4.1. Porosity and microstructure

The thermal behaviors of the sugarcane bagasse and rice husk PFAs utilized in this study are shown in the thermogravimetric plot of Fig. 3a. Four stages can be distinguished in the weight loss process of rice husk and sugarcane bagasse: (i) removal of moisture and extremely volatile components (<120 °C); (ii) hemicellulose decomposition (220–315 °C); (iii) lignin and cellulose decomposition (315–400 °C); and (iv) lignin decomposition (>450 °C) [52,53]. Lignin decomposition, on the other hand, proceeds more slowly and over a larger temperature range of 180–900 °C [54]. It is also important to note that after the decomposition process, the ash content levels in the two samples varied. Compared to rice husk, which had a residue of roughly 28% silica (SiO_2) known as rice husk ash (RHA), sugarcane bagasse had almost no ash. A comparable range of RHA value (13–29%) was observed in another investigation [55]. Therefore, the organic burnout method in this work was optimized and depended on the weight loss properties of rice husk and sugarcane bagasse in order to generate defect-free porous alumina ceramics.

While new phases of nickel alumosilicate ($N_3Al_2SiO_8$) spinelloid and nickel aluminate ($NiAl_2O_4$) spinel were observed in the RH and SCB derived composites, it is clear from the results of the XRD (Fig. 3b) that the corundum and cristobalite (resulting from RHA in the RH-derived porous alumina) phases in the monolithic samples are absent. Equations (9) and (10) show, respectively, the chemical reactions that result in the creation of the $NiAl_2O_4$ spinel and $N_3Al_2SiO_8$ spinelloid. Nevertheless, as was previously mentioned elsewhere [56], it is crucial to note that the existence of minimal ferrierite phase in the composites was caused by the trapped H_2O gas in addition to the substantial affinity of hydrated Ni^{+} for the tectosilicate (ferrierite) group.

$$Ni + Al_2O_3 + \frac{1}{2}O_2 \leftrightarrow NiAl_2O_4 \tag{9}$$

$$3NiO + Al_2O_3 + SiO_2 \leftrightarrow NiAl_2O_4\ .Ni_2SiO_4 \leftrightarrow Ni_3Al_2SiO_8 \tag{10}$$

As shown in Fig. 3c, porosity increased with increasing PFA content in both sample types from 5 to 15 wt% due to the development of a hierarchical porosity gradient in relation to increasing PFA-matrix ratio in the samples. Because the hard-textured rice husk particles prevented the alumina grains from densifying, RH-derived porous alumina generally exhibited more porosity than its SCB-derived counterparts (see Fig. 1a and b). Meanwhile, when nickel reinforcement increased, the porosity of the two sample grades also rose. It is noteworthy that the low wettability and thermal expansion difference between the initial Al_2O_3 matrix (8.1 x 10^{-6} m/mk) and the Ni reinforcing metal (13 x 10^{-6} m/mk) hindered the simultaneous processes of densification and spinellization in the course of sintering [57]. Thus, increasing Ni reinforcement causes the porosity to increase. The generated $N_3Al_2SiO_8$ spinelloid, which aided in the densification mechanism and restricted the porosity of the intergranular matrix in this group of composites, is responsible for the RH-derived composites' lower porosity when compared to their SCB-derived counterparts.

In fact, it is believed that the developed $N_3Al_2SiO_8$ spinelloid will greatly improve the chemical stability (explained in more detail in the

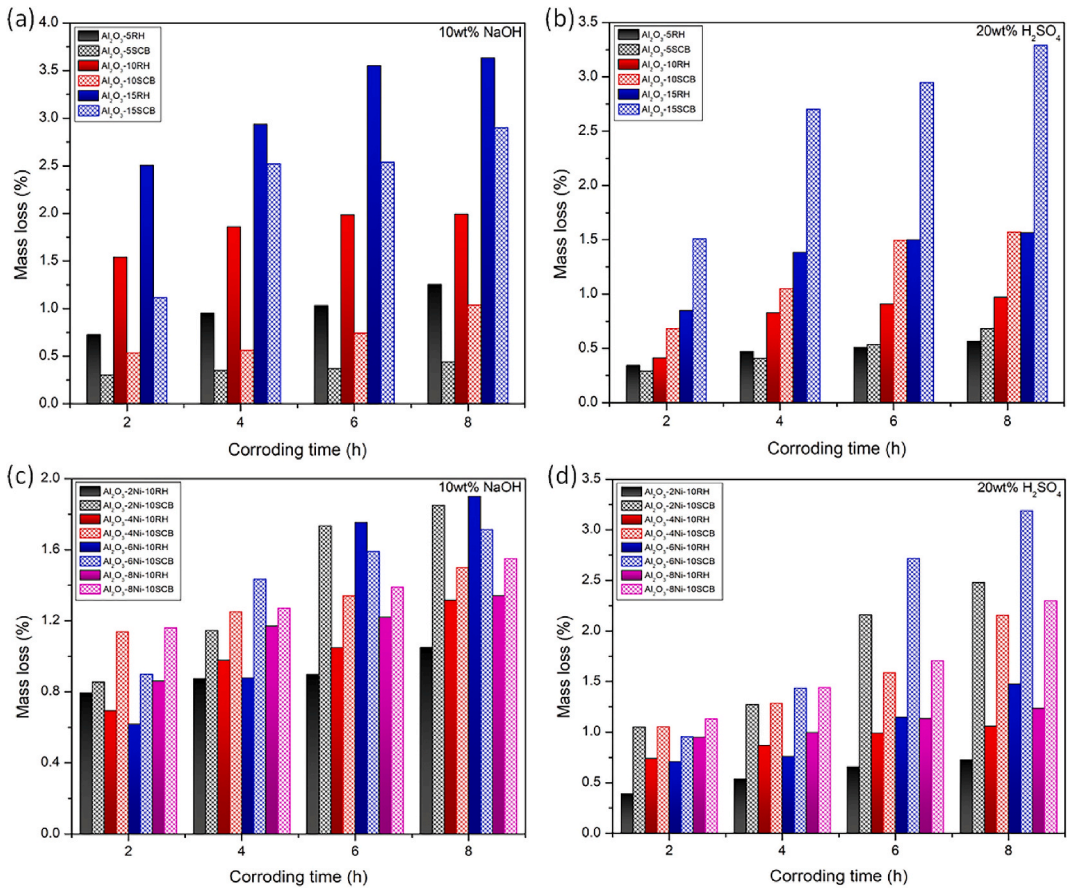

Fig. 6. Mass loss of monolithic and Ni-reinforced porous alumina after various durations in (a,c) alkali, and (b,d) acid solutions.

following section) of the RH-derived composites in corrosive environments when compared to their monolithic and SCB-derived counterparts. The pores cavities from the FESEM microstructures were characterized using microscopic image analysis to measure the pore size as presented in Fig. 3d. As expected, the pore size increased with increasing contents of pore formers and Ni-reinforcement in the monolithic and Ni-reinforced samples, respectively. More so, the sizes of pores retained in RH-graded samples are way higher than their corresponding SCB-graded counterparts. This result is best explained by the inherent textural characteristics of the pore-forming agents, since the rice husk particles' harder texture than sugarcane bagasse's prevented the former from disintegrating during the exploited processing route.

The microstructures of the porous ceramics generated from rice husk and sugarcane bagasse are shown in Figs. 4 and 5, respectively. The pore cavities displayed by the composite samples clearly have similar morphologies to those of their monolithic counterparts, as shown in Fig. 4(a and b) and 5(a,b). Furthermore, as the EDS elemental maps in Fig. 4c illustrate, the $Ni_3Al_2SiO_8$ spinelloid in the RH-derived porous composite was produced by the sintering of the original materials with the involvement of an additional phase of silica that was retained during the process. The bright-field FETEM microstructures of the RH and SCB derived porous ceramic composites exhibit varying degrees of intercalated Ni particles, or dark particles, on the surfaces of the matrix alumina grains that correspond to the $Ni_3Al_2SiO_8$ spinelloid and the $NiAl_2O_4$ spinel identified in the crystallographic patterns.

The morphology (Fig. 4d) of the RH-derived sample shows a refined grain structure (0.4–0.9 μm) and a significantly superior spinel coating, indicating good wettability of the Ni particles, higher densification, and lower granular porosity. This is further supported by the SAED pattern (inset), which shows considerable electron diffraction and indicates that this sample grade contains a fairly substantial number of polycrystalline phases of both nickel and silica. Additionally, as shown in the EDS spectrum (Fig. 4f) of spot A (Fig. 4e), silica retention in the RH-derived sample activated the interlocking of the $Ni_3Al_2SiO_8$ spinelloid interface with the amorphous grain. The SCB-derived porous composite, on the other hand, exhibits a severely limited dispersion of the Ni phase, which in turn raises the possibility of a partially flawed $NiAl_2O_4$ spinel crystallization (Fig. 5c). In addition, defects are also generated, such as broader granular porosity, undesirable grain growth (0.7–1.5 μm), and the coalescence of nickel particles at the periphery of the spinel precipitated grains (Fig. 5d).

4.2. Corrosion resistance

The mass loss as a function of corrosion time is shown in Fig. 6 for the monolithic and composite samples obtained from RH and SCB pore forming agents. Similar to their corresponding monolithic counterparts, the mass loss of the composites increased with greater duration in the hot acidic and alkaline solutions, regardless of the pore former type. Additionally, it is clear from the plots that different porous ceramic grades (RH and SCB) maintained similar patterns of corrosion resistance when compared to their monolithic counterparts after corrosion, with the RH and SCB derived porous ceramics demonstrating better resistance to chemical attack in hot 20 wt% H_2SO_4 and 10 wt% NaOH solutions, respectively.

Irrespective of the sample grade, a sharp rise in the percent mass loss of the monolithic samples prepared with PFA contents of 5–15 wt% can be evidenced. Porosity and corrosion rate can therefore be inferred to be directly related. More specifically, the enhanced porosity-associated quick dissolving rate results from both the severe crystal grain exfoliation from fragile sintering necks and the attacking fluid's ease of passage via the expanding interconnected pore space. The percent mass loss of

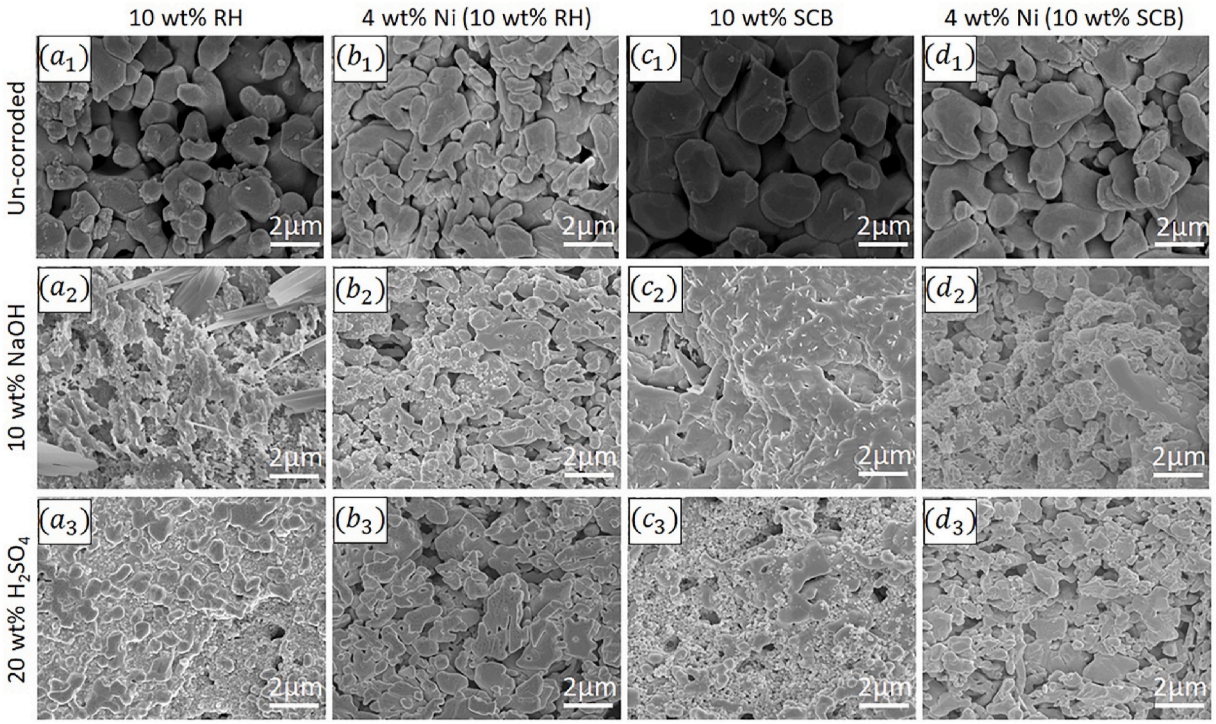

Fig. 7. FESEM microstructures of both (a,c) monolithic porous alumina and (b,d) Ni-reinforced porous alumina after corrosion for 8h in different media. Subscripts 1, 2 and 3 denote un-corroded, 10 wt% NaOH and 20 wt% H_2SO_4, respectively.

both sample grades for the composites also rose with increasing Ni reinforcement. This finding aligns with research conducted elsewhere, which established a relationship between the physical features of porous ceramics, including criteria for porosity and density, and the resistance to corrosion in any liquid medium [58,59].

Furthermore, the RH-derived monolithic and Ni-reinforced porous ceramics showed greater corrosion resistance in strong acid as compared to the strong alkali solution, although their SCB counterparts showed a divergent pattern. Clearly, the findings of Nickel and Seipel [60] provide additional evidence that the presence of glassy grain boundaries dominated by secondary silica phase increased the susceptibility of the monolithic RH-derived porous ceramics in hot alkali media. The comparatively minimal % mass loss reported for the composite equivalents, in contrast to the corresponding monolithic sample prepared with 10 wt% PFA, is best explained by: (i) the viscosity of the liquid medium, which increased due to the $Ni_3Al_2SiO_8$ spinelloid's capacity to accommodate cations (Na^+) from the corrosion medium on its cation sites (Al^{3+} and Si^{4+}) preventing the hot NaOH solution from quickly infiltrating the composite samples, and (ii) the $Ni_3Al_2SiO_8$ spinelloid reaction with the NaOH medium (supported by Eq. (11)) stimulated the generation of sodium silicate (Na_2SiO_3) layer, serving as a hindrance to the samples' continued disintegration in the medium.

$$Ni_3Al_2SiO_8 + 4NaOH + H_2O \leftrightarrow 3Ni(OH)_2 + Na_2SiO_3 + 2NaAlO_2 \quad (11)$$

with the exception of the RH-derived composite prepared with 2 wt% Ni, the other composites' flawed performance in strong acid solution compared to their monolithic counterpart can be attributed to inadequate spinel crystallization, impaired densification, and an increase in porosity with rising nickel content. When compared to their RH- and SCB-derived monolithic sample with 10 wt% PFA counterparts, the SCB-graded composites performed poorly in the two corrosive media. The continuous development of poorly crystallized $NiAl_2O_4$ spinel and the impact of comparatively high porosity values with increased Ni reinforcement were the main factors responsible for this. This is in contrast to how much SiO_2 retention affected how well the RH-derived porous alumina composites performed in the corrosion media compared to their monolithic counterparts. The microstructures of the monolithic and Ni-reinforced porous alumina, both uncorroded and corroded, are shown in Fig. 7. Similar to their monolithic counterparts, exfoliated crystal-like formations developed on the surface of the composites regardless of the corrosion medium employed. In addition, the formation of the $Ni_3Al_2SiO_8$ spinelloid, despite the crystal exfoliation, supported the microstructure stability of the samples derived from RH as opposed to those derived from SCB, where additional surface fissures were noticed due to the dissolution of the extremely susceptible $NiAl_2O_4$ spinel phase.

5. Machine learning methods

The computational analysis' goal is to develop two models, XGBoost and Jaya-XGBoost that can predict the corrosion-induced mass loss of monolithic and nickel-reinforced porous alumina ceramics in hot aqueous solutions (110 °C) containing 10 wt% NaOH and 20 wt% H_2SO_4. The dataset utilized to create the models' algorithms was obtained from the experimental study in our earlier investigation [33,35]. The collection contains 112 distinct data patterns. Five input variables (rice husk loading, sugarcane bagasse loading, nickel reinforcement loading, porosity value, and corrosion duration) and two output parameters (mass loss in NaOH and mass loss in H_2SO_4) were derived from this database to build the models examined in this work. The following two significant experiments provided the basis for the model development framework that was suggested. The primary objective of the first experiment is to evaluate the prediction performance of the XGBoost technique for the mass loss values of monolithic and nickel-reinforced porous alumina ceramics in various corrosion conditions, throughout the whole original dataset. The second experiment aims to assess the effectiveness of the suggested Jaya-XGBoost method, which uses an automatic data detection and model selection-oriented optimization process, in improving the XGBoost model's accuracy. The MATLAB r2021b environment, a laptop with a 12th Gen Intel ® Core i7-1255U 2.60 GHz CPU, and 16 GB of installed RAM were used to carry out the given experiments.

Table 1
Hyper-parameters of XGBoost decision tree model.

Hyper-parameters	Initial value	[Test range] (increment size)	Control value
Number of trees	40	[1200] (10)	120
Learning rate	0.2	[0.01, 0.05, 0.07, 0.1, 0.2, 0.5, 1, 2, 4]	0.1
Max-depth	4	[3,10] (1)	5
Min-child-weight	5	[1,10] (1)	5
Subsample	0.6	[0.1, 1.0] (0.1)	0.8
Colsample-bytree	0.6	[0.1, 1.0] (0.1)	0.5
γ	0	[0, 0.6] (0.1)	0
λ	1	[0, 0.05, 0.1, 1, 2, 3, 4]	1
[a]	0	[0, 0.05, 0.1, 1, 2, 3, 4]	0

5.1. Predictive performance of XGBoost model

Changes in the behavior of the XGBoost machine become evident when adjusting various initial hyper-parameters such as the number of trees, learning rate, maximum depth, minimum child weight, subsample ratio, colsample ratio, as well as regularization factors γ, α, and λ. The number of trees reflects the number of regression trees in the XGBoost model; the learning rate determines the step size for each training round; maximum depth controls the tree's complexity by defining the number of branches from the root to the leaf; minimum child weight influences the complexity of the tree, with lower values leading to potentially overfitted models; subsample indicates the portion of the training set used in each tree; colsample ratio defines the proportion of attributes considered in each tree; and γ, α, and λ serve as regularization factors, employed to counter overfitting tendencies in the model [44]. Table 1 illustrates appropriate selections of hyperparameters of the XGBoost decision tree model by trial and error.

Two portions of the dataset were taken: 75% (84 data patterns) were utilized for training, and the remaining 25% (28 data patterns) were utilized for testing. The variations in training, validation, and testing criteria are shown in Table 2. The table shows that as the number of trees in the XGBoost model increased, the mean values of the training, validation, and testing set R^2 shifted. The R^2 values for the XGBoost model's training, validation, and testing sets show appreciable variations based on these data. Moreover, it is clear that the mean values of RMSE and MAE are substantially near to one another when compared to other error values in Table 2.

5.2. Predictive performance of Jaya-XGBoost model

This experiment was conducted to evaluate the effectiveness of the proposed Jaya-XGBoost model in enhancing the accuracy of the XGBoost model through an automatic data detection and model selection-oriented optimization process. It is essential to emphasize how the Jaya algorithm is distinct from a few well-known heuristic algorithms, which call for both common and unique control parameters. These algorithms include the genetic algorithm (GA), differential evolution (DE), particle swarm optimization (PSO), and moth-flame optimization [61]. Nevertheless, the Jaya method just uses general control parameters, such as population size and number of generations, and does not rely on any algorithm-specific parameters. Regarding the hybrid model built on XGBoost, Jaya aims to optimize parameters such as

Table 2
Performance of XGBoost under different numbers of trees.

Tree-number	Training			Validation			Testing		
	R^2	RMSE	MAE	R^2	RMSE	MAE	R^2	RMSE	MAE
20	0.9048	0.1069	0.0763	0.8047	0.1243	0.1141	0.8065	0.1369	0.1040
30	0.9074	0.1016	0.0600	0.6412	0.1787	0.1267	0.9012	0.0438	0.0355
50	0.9760	0.0188	0.0143	0.9721	0.0216	0.0176	0.9664	0.0089	0.0085
60	0.9559	0.0920	0.0401	0.9663	0.0229	0.0211	0.9013	0.0786	0.0495
70	0.8684	0.0934	0.0719	0.9486	0.1312	0.1089	0.6825	0.1113	0.0884
80	0.9202	0.0574	0.0283	0.9726	0.0430	0.0356	0.9225	0.0243	0.0137
100	0.8943	0.0901	0.0652	0.8567	0.0843	0.0645	0.8903	0.1609	0.1180
110	0.9442	0.0785	0.0573	0.9166	0.0531	0.0368	0.9153	0.0883	0.0685
120	0.9757	0.0356	0.0294	0.9674	0.0421	0.0263	0.9445	0.0466	0.0353
140	0.9679	0.0464	0.0343	0.9284	0.0849	0.0637	0.9334	0.0260	0.0214
160	0.9312	0.0271	0.0199	0.7347	0.0907	0.0576	0.9258	0.1943	0.1371
170	0.9274	0.0544	0.0378	0.9234	0.0688	0.0453	0.9771	0.0427	0.0357
180	0.9662	0.0662	0.0411	0.8952	0.0271	0.0165	0.9216	0.0300	0.0220
200	0.8811	0.1034	0.0858	0.9329	0.0671	0.0458	0.9413	0.0917	0.0739

Table 3
Performance of Jaya-XGBoost based on parameter optimizations.

Iteration	Fitness value	Training			Testing			Tree-number
		R^2	RMSE	MAE	R^2	RMSE	MAE	
1	0.9369	0.9157	0.0982	0.0701	0.8163	0.1257	0.0955	20
2	0.9434	0.9185	0.0933	0.0551	0.9122	0.0402	0.0326	9
3	0.9506	0.9766	0.0173	0.0132	0.9753	0.00821	0.0078	18
4	0.9469	0.967	0.0845	0.0369	0.9123	0.0721	0.0454	14
5	0.9367	0.8789	0.0858	0.0661	0.6908	0.1022	0.0812	11
6	0.9301	0.931	0.0528	0.0261	0.9328	0.0223	0.0126	22
7	0.9209	0.9052	0.0827	0.0599	0.9010	0.1478	0.1084	9
8	0.9538	0.9556	0.0721	0.0527	0.9265	0.0811	0.0635	12
9	0.9643	0.9774	0.0327	0.0269	0.9559	0.0428	0.0324	15
10	0.9725	0.9765	0.0426	0.0314	0.9448	0.0238	0.0196	**17**
11	0.9571	0.9424	0.0249	0.0182	0.9369	0.1785	0.1260	10
12	0.9350	0.9386	0.0501	0.0347	0.9754	0.0392	0.0329	18
13	0.9692	0.9725	0.0609	0.0378	0.9327	0.0275	0.0202	28
14	0.9270	0.8918	0.0950	0.0789	0.9528	0.0842	0.0679	24

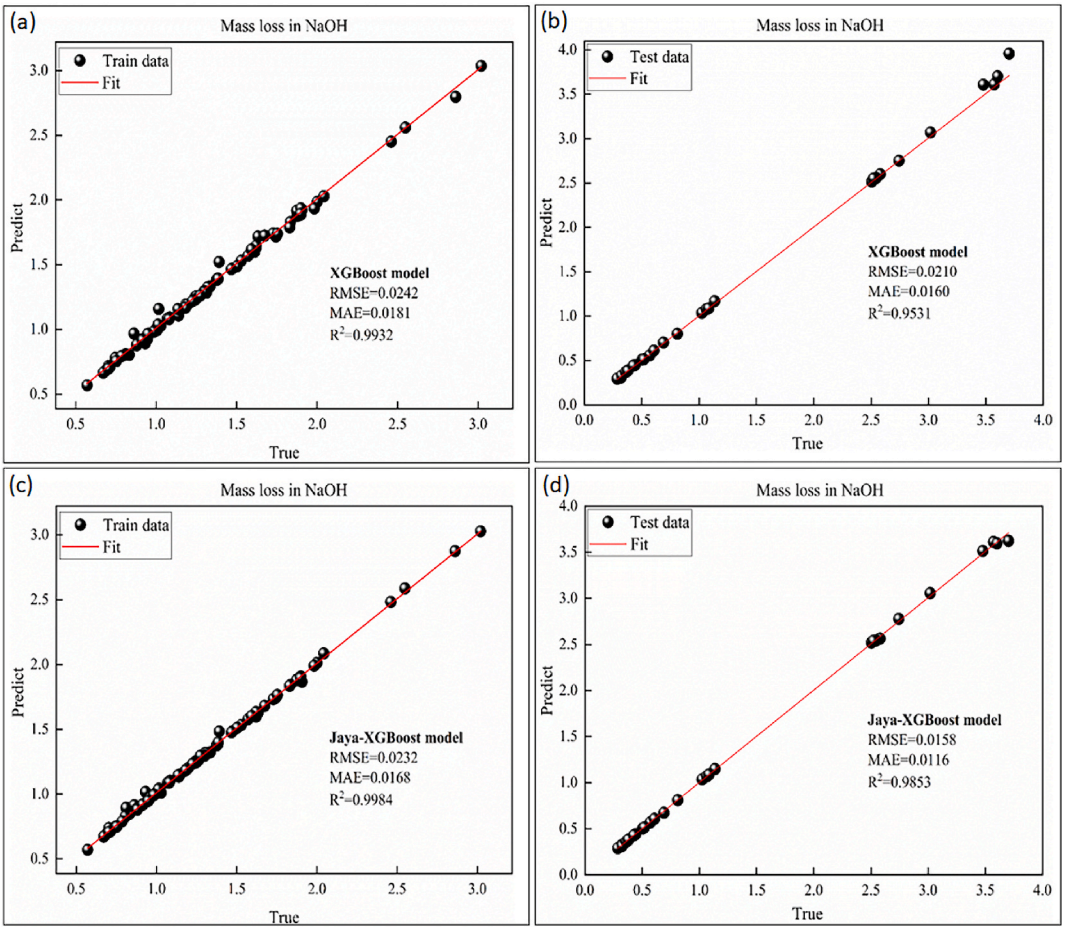

Fig. 8. Comparison of predicted and experimental (True) values for mass loss in NaOH using XGBoost and Jaya- XGBoost models.

"num_boosting_rounds," "learning_rate," and "reg_lambda" in XGBoost. In the process of optimization, the ranges of parameters are specified as (1–200), (0.0001–1), and (0.001–10), respectively. Several experiments revealed that when the number of iterations increased, too many swarms would cause computation time to increase, while too few swarms would cause fitness values in each optimization step to fluctuate. Consequently, after ten independent runs, the number of iterations and population size were changed to 14 and 50, respectively. The optimal parameters were determined as follows: "*num_boosting_round*" = 128; "*learning_rate*" = 0.4874; and "*reg_lambda*" = 0.0768.

The optimal tree-number and selected data for Jaya-XGBoost are shown in Table 3. The best results at a specific iteration and the corresponding tree-number are highlighted in bold as the best solution.

5.3. Performance comparison

The comparative plots illustrating the experimental and predicted results using the Jaya-XGBoost and XGBoost for mass loss in NaOH and mass loss in H_2SO_4 are depicted in Figs. 8 and 9. Panels a and c represent the results for the training set, while panels b and d represent the results for the testing set. Clearly visible from the figures, most of the data points in the training set for both models are distributed on both sides of the fitted line, as indicated by R^2 values. This suggests that both models exhibit a strong fitting ability. For both the training and testing datasets, the researched Jaya-XGBoost model outperforms XGBoost in terms of R^2 fitting ability. Notable is also the fact that the training dataset has a substantially higher R^2 than the testing dataset.

Analyzing the performance metrics of each model reveals that the Jaya-XGBoost model outperformed the conventional XGBoost model. For the prediction of mass loss in NaOH, the XGBoost model achieved R^2 and RMSE values of 0.9932 and 0.0242, respectively, while the Jaya-XGBoost model generated 0.9984 and 0.0232, respectively. In a similar way, the XGBoost model achieved R^2 and RMSE values of 0.9773 and 0.0287, accordingly, for the prediction of mass loss in H_2SO_4, whereas the Jaya-XGBoost model produced values of 0.9824 and 0.0273, respectively. It is commonly acknowledged that a low RMSE value indicates a high success rate for the method [35]. The RMSE value signifies the average difference between the predicted value and the real value, and a smaller RMSE value corresponds to higher model accuracy. Therefore, the superior prediction capacity demonstrated by the Jaya-XGBoost model (Fig. 10) is attributed to the incorporation of the Jaya optimizer algorithm.

The proposed Jaya-XGBoost performance surpasses those of Wang et al. [62] and Abdullah et al. [63] on the prediction of corrosion susceptibility of high strength concrete subjected to different chemical attacks, where R^2 of 0.87 and 0.9379, respectively were obtained for the single XGBoost models. The proposed Jaya-XGBoost model has proven to be able to accurately predict the behavior of corrosion resistance in both monolithic and nickel-reinforced porous alumina ceramics, as well as effectively control the material selection process. This is supported by the figures, which demonstrate a strong fit between the predicted and experimental results. Thus, it can be concluded that by employing available data for the prediction of the corrosion resistance behavior of the materials, the models developed in this work, especially the Jaya-XGBoost algorithm, can have benefits in terms of cutting down on the time and cost of experimental testing of porous ceramic materials under various harsh chemical environments.

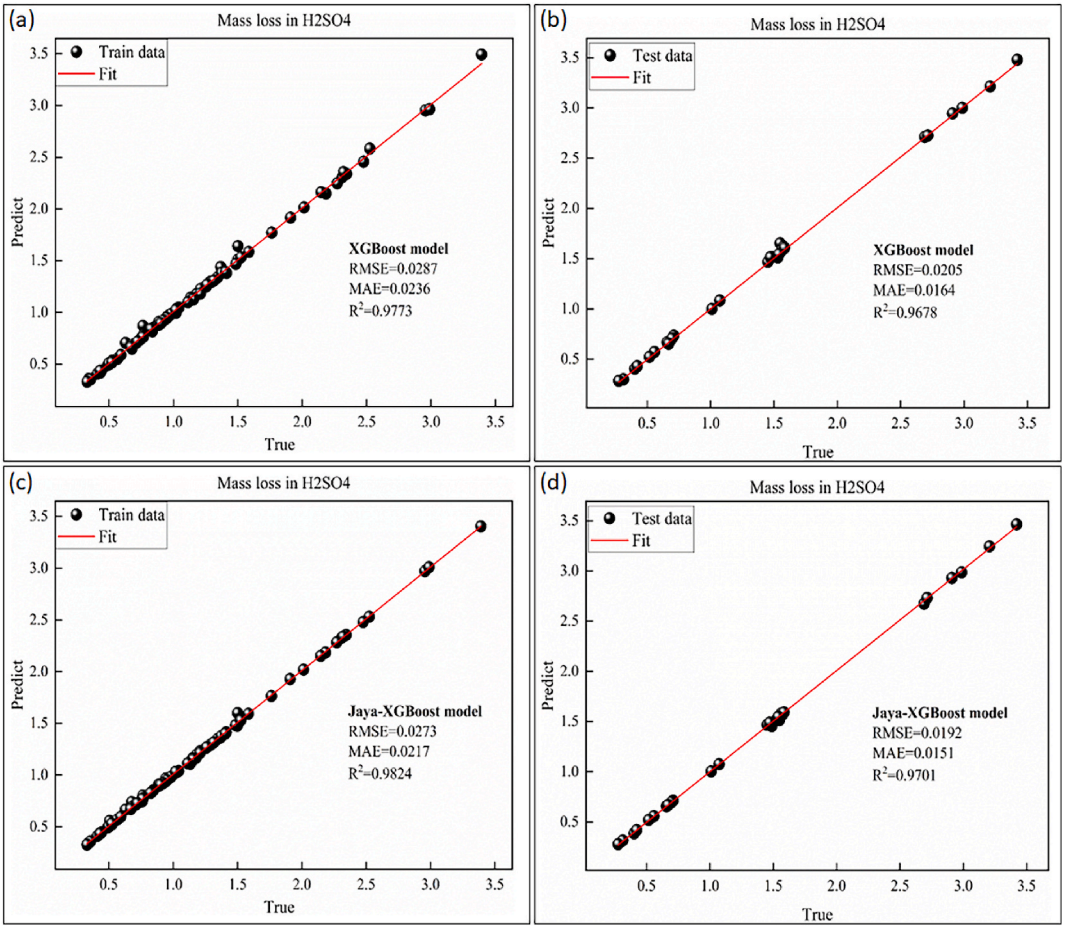

Fig. 9. Comparison of predicted and experimental (True) values for mass loss in H_2SO_4 using XGBoost and Jaya- XGBoost models.

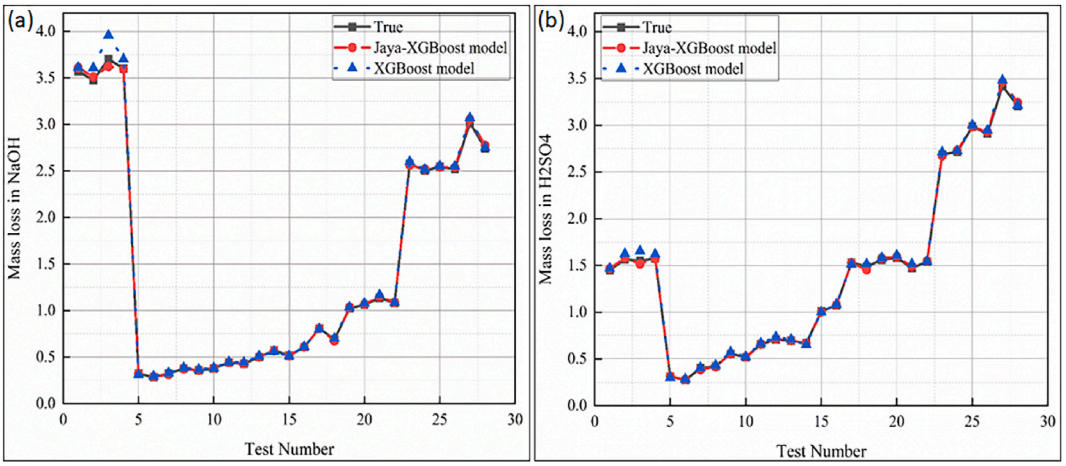

Fig. 10. Comparison of data for mass loss in NaOH and mass loss in H_2SO_4 using XGBoost and the Jaya-XGBoost models.

6. Conclusions

A rapidly developing technique to reduce the time required for reliability testing of new and advanced materials is machine learning, which is based on statistics and large data. Large-scale experimentation to determine compatibility in a variety of industrial processes requiring harsh service conditions has been the main focus of the majority of prior investigations on the corrosion behavior of porous ceramics. In this study, however, we employed a hybridized machine learning prediction model called Jaya-XGBoost to predict the corrosion-induced mass loss of monolithic and nickel-reinforced porous alumina ceramics. Empirical findings showed that the emergence of a very stable $Ni_3Al_2SiO_8$ spinelloid phase in the RH-graded composites was responsible for improving their chemical stability in both the 10 wt% NaOH and 20 wt% H_2SO_4 corrosive environments compared to their monolithic and corresponding SCB-graded counterparts. Whereas, an abysmal performance was demonstrated by the SCB-graded composites in both corrosive media in contrast to their plain counterpart due to the existence of poorly

crystallized $NiAl_2O_4$ spinel. Thus, the kind of agro-waste PFA used provides insights into the ideal operating conditions that can provide the best possible performance and chemical stability for the developed porous ceramics. These specimens' corrosion test results were gathered and fitted into the machine learning algorithms of XGBoost and Jaya-XGBoost. Based on statistical accuracy criteria, the Jaya-XGBoost model outperformed the normal XGBoost model in predicting the corrosion-induced mass loss of both the monolithic and nickel-reinforced porous alumina. For the prediction of mass loss in NaOH, the XGBoost model achieved R^2 and RMSE values of 0.9932 and 0.0242, respectively, whereas the Jaya-XGBoost model achieved values of 0.9984 and 0.0232, respectively. Similarly, for the prediction of mass loss in H_2SO_4, the XGBoost model yielded R^2 and RMSE values of 0.9773 and 0.0287, respectively, while the Jaya-XGBoost model provided values of 0.9824 and 0.0273, respectively. The proposed model can be used as a decision support system by design engineers working in the field of macroporous ceramics to assess the corrosion resistance capabilities of novel porous ceramic systems formed using PFAs from agricultural waste.

Data availability

Data will be made available on request.

Declaration of competing interest

The authors declare that they have no known competing financial interests or personal relationships that could have appeared to influence the work reported in this paper.

Acknowledgement

This work was supported by Tenaga Nasional Berhad (TNB) and UNITEN through the BOLD Refresh Postdoctoral Fellowships under the project code of J510050002-IC-6 BOLDREFRESH2025-Centre of Excellence and Universiti Putra Malaysia (UPM) Research Grant (UPM/GP-IPB/2020/9688700). This research was also funded by the Brain Pool program of the Ministry of Science and by ICT through the National Research Foundation of Korea (RS-2023-00218940).

References

[1] Oyekanmi AA, Khalil HA, Dele-Afolabi TT, Rafatullah M, Mohammed RM, Alfatah T, Mohammed D, Abdullah CK. Fabrication and characterization of porous ceramic composite membrane for water and wastewater treatment. Desalination Water Treat 2022;246:174–95. https://doi.org/10.5004/dwt.2022.28031.

[2] Tishkevich DI, Vorobjova AI, Bondaruk AA, Dashkevich ES, Shimanovich DL, Razanau IU, Zubar TI, Yakimchuk DV, Dong MG, Sayyed MI, Somaily HH. The interrelation of synthesis conditions and wettability properties of the porous anodic alumina membranes. Nanomaterials 2022;12(14):2382. https://doi.org/10.3390/nano12142382.

[3] Vorobjova AI, Tishkevich DI, Outkina EA, Shimanovich DL, Razanau IU, Zubar TI, Bondaruk AA, Zheleznova EK, Dong M, Aloraini DA, Sayyed MI. A study of Ta2O5 nanopillars with Ni tips prepared by porous anodic alumina through-mask anodization. Nanomaterials 2022;12(8):1344. https://doi.org/10.3390/nano12081344.

[4] Gu Q, Ng TC, Bao Y, Ng HY, Tan SC, Wang J. Developing better ceramic membranes for water and wastewater Treatment: where microstructure integrates with chemistry and functionalities. Chem Eng J 2022;428:130456. https://doi.org/10.1016/j.cej.2021.130456.

[5] Bera SP, Godhaniya M, Kothari C. Emerging and advanced membrane technology for wastewater treatment: a review. J Basic Microbiol 2022;62(3–4):245–59. https://doi.org/10.1002/jobm.202100259.

[6] Baig U, Waheed A. An efficient and simple strategy for fabricating a polypyrrole decorated ceramic-polymeric porous membrane for purification of a variety of oily wastewater streams. Environ Res 2023;219:114959. https://doi.org/10.1016/j.envres.2022.114959.

[7] Sadek AH, Abdel-Karim A, Mohsenpour S, Ismail SH, Bayoumy AM, Ibrahim M, Mohamed GG. Polysulfone-based mixed matrix membranes loaded with a multifunctional hierarchical porous Ag-Cu dendrites@ SiO2 core-shell nanostructure for wastewater treatment. Process Saf Environ Protect 2023;175:677–91. https://doi.org/10.1016/j.psep.2023.05.085.

[8] Sawunyama L, Oyewo OA, Seheri N, Onjefu SA, Onwudiwe DC. Metal oxide functionalized ceramic membranes for the removal of pharmaceuticals in wastewater. Surface Interfac 2023;38:102787. https://doi.org/10.1016/j.surfin.2023.102787.

[9] Chen H, Pan Y, Chen B, Li J, Gui Z, Chen J, Yan H, Zeng Y, Chen J. Fabrication of porous aluminum ceramics beyond device resolution via stereolithography 3D printing. Ceram Int 2023;49(11):18463–9. https://doi.org/10.1016/j.ceramint.2023.02.218.

[10] Alzukaimi J, Jabrah R. Development of high strength large open porosity alumina ceramics using the sacrificial phase route: the role of the sacrificial phase fineness. Ceram Int 2023;49(2):2923–33. https://doi.org/10.1016/j.ceramint.2022.09.277.

[11] Li X, Yan L, Guo A, Du H, Hou F, Liu J. Lightweight porous silica-alumina ceramics with ultra-low thermal conductivity. Ceram Int 2023;49(4):6479–86. https://doi.org/10.1016/j.ceramint.2022.10.165.

[12] Krishnan PR, Kumar PA, Prabhakaran K. Preparation of macroporous alumina ceramics by ice templating without freeze drying using natural rubber latex binder. J Porous Mater 2023;30(5):1499–507. https://doi.org/10.1007/s10934-023-01437-z.

[13] Suleiman B, Zhang H, Ding Y, Li Y. Microstructure and mechanical properties of cold sintered porous alumina ceramics. Ceram Int 2022;48(10):13531–40. https://doi.org/10.1016/j.ceramint.2022.01.232.

[14] Wang Y, Ma B, Ulbricht M, Dong Y, Zhao X. Progress in alumina ceramic membranes for water purification: status and prospects. Water Res 2022;226:119173. https://doi.org/10.1016/j.watres.2022.119173.

[15] Bakhtierkhalzi M, Islam MW, Suzauddin M, Islam MN, Al Mahmood A. Effect of TiO2 as sintering additive on microstructural, physical, and mechanical properties of CeO2 doped zirconia toughened alumina ceramic composite. Ceram Int 2023;49(4):6666–70. https://doi.org/10.1016/j.ceramint.2022.10.282.

[16] Li H, Yang F, Zhang BX, Guo Y, Han W, Zhao T, Qiu W. Preparation and characterization of Nextel 720/alumina ceramic matrix composites via an improved prepreg process. Int J Appl Ceram Technol 2022;19(4):1970–80. https://doi.org/10.1111/ijac.14037.

[17] Lieberthal M, Kaplan WD. Processing and properties of Al2O3 nanocomposites reinforced with sub-micron Ni and NiAl2O4. Mater Sci Eng, A 2001;302(1):83–91. https://doi.org/10.1016/S0921-5093(00)01358-7.

[18] Sekino T, Nakajima T, Ueda S, Niihara K. Reduction and sintering of a nickel–dispersed-alumina composite and its properties. J Am Ceram Soc 1997;80(5):1139–48. https://doi.org/10.1111/j.1151-2916.1997.tb02956.x.

[19] Dele-Afolabi TT, Hanim MA, Norkhairunnisa M, Sobri S, Calin R, Ismarrubie ZN. Significant effect of rice husk and sugarcane bagasse pore formers on the microstructure and mechanical properties of porous Al2O3/Ni composites. J Alloys Compd 2018;743:323–31. https://doi.org/10.1016/j.jallcom.2018.01.230.

[20] Dele-Afolabi TT, Hanim MA, Norkhairunnisa M, Sobri S, Calin R, Ojo-Kupoluyi OJ. Effect of nickel addition on the microstructure and corrosion resistance properties of porous alumina composites shaped with sugarcane bagasse pore-forming agent. IOP Conf Ser Mater Sci Eng 2019;469(1):012019. https://doi.org/10.1088/1757-899X/469/1/012019.

[21] Fung YL, Wang H. Investigation of reinforcement of porous alumina by nickel aluminate spinel for its use as ceramic membrane. J Membr Sci 2013;444:252–8. https://doi.org/10.1016/j.memsci.2013.05.025.

[22] Fung YL, Wang H. Nickel aluminate spinel reinforced ceramic hollow fibre membrane. J Membr Sci 2014;450:418–24. https://doi.org/10.1016/j.memsci.2013.09.036.

[23] Shih K, Leckie JO. Nickel aluminate spinel formation during sintering of simulated Ni-laden sludge and kaolinite. J Eur Ceram Soc 2007;27(1):91–9. https://doi.org/10.1016/j.jeurceramsoc.2006.04.176.

[24] Shih K, White T, Leckie JO. Nickel stabilization efficiency of aluminate and ferrite spinels and their leaching behavior. Environ Sci Technol 2006;40(17):5520–6. https://doi.org/10.1021/es0601033.

[25] He Y, Shih K. Nano-indentation on nickel aluminate spinel and the influence of acid and alkaline attacks on the spinel surface. Ceram Int 2012;38(4):3121–8. https://doi.org/10.1016/j.ceramint.2011.12.013.

[26] Rotkovich AA, Tishkevich DI, Razanau IU, Vershinina TN, Bondaruk AA, German SA, Zubar TI, Sayyed MI, Dong M, Yao Y, Mahmoud KA. Development and study of lightweight recycled composite materials based on linear low-density polyethylene and W for radiation application. J Mater Res Technol 2024;30:1310–8. https://doi.org/10.1016/j.jmrt.2024.03.187.

[27] Tishkevich DI, Zubar TI, Zhaludkevich AL, Razanau IU, Vershinina TN, Bondaruk AA, Zheleznova EK, Dong M, Hanfi MY, Sayyed MI, Silibin MV. Isostatic hot pressed W–Cu composites with nanosized grain boundaries: microstructure, structure and radiation shielding efficiency against gamma rays. Nanomaterials 2022;12(10):1642. https://doi.org/10.3390/nano12101642.

[28] Liu J, Ren B, Lu Y, Xi X, Li Y, Liu K, Yang J, Huang Y. Novel design of elongated mullite reinforced highly porous alumina ceramics using carbonized rice husk as pore-forming agent. Ceram Int 2019;45(11):13964–70. https://doi.org/10.1016/j.ceramint.2019.04.095.

[29] Rumaizah CZ, Fazureen A, Razali MH, Asmadi A, Muhamad Nor MA. Properties and filtration performance of porous clay membrane produced using sawdust as pore forming agent. Key Eng Mater 2019;821:337–42. https://doi.org/10.4028/www.scientific.net/KEM.821.337.

[30] Wahsh MM, Mansour TS, Othman AG, Bakr IM. Recycling bagasse and rice hulls ash as a pore-forming agent in the fabrication of cordierite–spinel porous ceramics. Int J Appl Ceram Technol 2022;19(5):2664–74. https://doi.org/10.1111/ijac.14082.

[31] Mohanta K, Kumar A, Parkash O, Kumar D. Processing and properties of low cost macroporous alumina ceramics with tailored porosity and pore size fabricated

using rice husk and sucrose. J Eur Ceram Soc 2014;34(10):2401–12. https://doi.org/10.1016/j.jeurceramsoc.2014.01.024.
[32] Permatasari N, Sucahya TN, Nandiyanto AB. Agricultural wastes as a source of silica material. Indonesian journal of science and technology 2016;1(1):82–106. https://ejournal.kjpupi.id/index.php/ijost/article/view/228.
[33] Dele-Afolabi TT, Hanim MA, Norkhairunnisa M, Sobri S, Calin R. Investigating the effect of porosity level and pore former type on the mechanical and corrosion resistance properties of agro-waste shaped porous alumina ceramics. Ceram Int 2017;43(12):8743–54. https://doi.org/10.1016/j.ceramint.2017.03.210.
[34] Liu P, Han Z, Wu W, Zhao Y, Song Y, Chai M. A developed convolutional neural network model for accurately and stably predicting effective thermal conductivity of gradient porous ceramic materials. Int J Heat Mass Tran 2024;225:125428. https://doi.org/10.1016/j.ijheatmasstransfer.2024.125428.
[35] Dele-Afolabi TT, Hanim MA, Norkhairunnisa M, Sobri S, Calin R, Ismarrubie ZN. Agro-waste shaped porous Al2O3/Ni composites: corrosion resistance performance and artificial neural network modelling. Mater Char 2018;142:77–85. https://doi.org/10.1016/j.matchar.2018.05.026.
[36] Karakoç A, Keleş Ö. A predictive failure framework for brittle porous materials via machine learning and geometric matching methods. J Mater Sci 2020;55(11):4734–47. https://doi.org/10.1007/s10853-019-04339-1.
[37] Swaminathan S, Shah T, Sirkeci-Mergen B, Keles O. Machine learning models for predicting fracture strength of porous ceramics and glasses. In: Proceedings of the 2018 international conference on data science; 2018.
[38] Nakai ME, Junior HG, Spadoto M. ANFIS applied to the prediction of surface roughness in grinding of advanced ceramics. In: Iasted conf. Artificial intelligence soft computing. vol. 30. Greece: Crete; 2011. p. 329–34.
[39] Mandal S, Pramanick A, Chakraborty S, Dey PP. ANFIS based model to forecast the Wire-EDM parameters for machining an Ultra High Temperature Ceramic composite. IOP Conf Ser Mater Sci Eng 2018;377(1):012088.
[40] Jiang D, Wang Z, Zhang J, Jiang D, Liu F, Hao L. Predictive modelling for contact angle of liquid metals and oxide ceramics by comparing Gaussian process regression with other machine learning methods. Ceram Int 2022;48(1):665–73. https://doi.org/10.1016/j.ceramint.2021.09.146.
[41] Kabiru OA, Owolabi TO, Ssennoga T, Olatunji SO. Performance comparison of SVM and ANN in predicting compressive strength of concrete. IOSR J Comput Eng 2014;16(5):88–94.
[42] Abd AM, Abd SM. Modelling the strength of lightweight foamed concrete using support vector machine (SVM). Case Stud Constr Mater 2017;6:8–15. https://doi.org/10.1016/j.cscm.2016.11.002.
[43] Friedman JH. Greedy function approximation: a gradient boosting machine. Ann Stat 2001:1189–232. https://www.jstor.org/stable/2699986.
[44] Chen T, Guestrin C. Xgboost: a scalable tree boosting system. InProceedings of the 22nd acm sigkdd international conference on knowledge discovery and data mining. 2016. p. 785–94. https://doi.org/10.1145/2939672.2939785.
[45] Torres-Barrán A, Alonso Á, Dorronsoro JR. Regression tree ensembles for wind energy and solar radiation prediction. Neurocomputing 2019;326:151–60. https://doi.org/10.1016/j.neucom.2017.05.104.
[46] Bui DK, Nguyen T, Chou JS, Nguyen-Xuan H, Ngo TD. A modified firefly algorithm-artificial neural network expert system for predicting compressive and tensile strength of high-performance concrete. Construct Build Mater 2018;180:320–33. https://doi.org/10.1016/j.conbuildmat.2018.05.201.
[47] Jaya Rao R. A simple and new optimization algorithm for solving constrained and unconstrained optimization problems. Int J Ind Eng Comput 2016;7(1):19–34. https://doi.org/10.5267/j.ijiec.2015.8.004.
[48] Abhishek K, Kumar VR, Datta S, Mahapatra SS. Application of JAYA algorithm for the optimization of machining performance characteristics during the turning of CFRP (epoxy) composites: comparison with TLBO, GA, and ICA. Eng Comput 2017;33:457–75. https://doi.org/10.1007/s00366-016-0484-8.
[49] Fahem N, Belaidi I, Brahim AO, Noori M, Khatir S, Wahab MA. Prediction of resisting force and tensile load reduction in GFRP composite materials using Artificial Neural Network-Enhanced Jaya Algorithm. Compos Struct 2023;304:116326. https://doi.org/10.1016/j.compstruct.2022.116326.
[50] Houssein EH, Gad AG, Wazery YM. Jaya algorithm and applications: a comprehensive review. Metaheuristics and optimization in computer and electrical engineering. 2021. p. 3–24. https://doi.org/10.1007/978-3-030-56689-0_2.
[51] Dele-Afolabi TT, Ahmadipour M, Hanim MA, Oyekanmi AA, Ansari MN, Sikiru S, Kumar N. Performance assessment of Sn-based lead-free solder composite joints based on extreme learning machine model tuned by Aquila optimizer. J Alloys Compd 2024;970:172684. https://doi.org/10.1016/j.jallcom.2023.172684.
[52] Sanchez-Silva L, López-González D, Villaseñor J, Sánchez P, Valverde JL. Thermogravimetric–mass spectrometric analysis of lignocellulosic and marine biomass pyrolysis. Bioresour Technol 2012;109:163–72. https://doi.org/10.1016/j.biortech.2012.01.001.
[53] Hashemi B, Sarker S, Lamb JJ, Lien KM. Yield improvements in anaerobic digestion of lignocellulosic feedstocks. J Clean Prod 2021;288:125447. https://doi.org/10.1016/j.jclepro.2020.125447.
[54] El-Sayed SA, Mostafa ME. Pyrolysis characteristics and kinetic parameters determination of biomass fuel powders by differential thermal gravimetric analysis (TGA/DTG). Energy Convers Manag 2014;85:165–72. https://doi.org/10.1016/j.enconman.2014.05.068.
[55] Krishnarao RV, Subrahmanyam J, Kumar TJ. Studies on the formation of black particles in rice husk silica ash. J Eur Ceram Soc 2001;21(1):99–104. https://doi.org/10.1016/S0955-2219(00)00170-9.
[56] Dalconi MC, Cruciani G, Alberti A, Ciambelli P, Rapacciuolo MT. Ni2+ ion sites in hydrated and dehydrated forms of Ni-exchanged zeolite ferrierite. Microporous Mesoporous Mater 2000;39(3):423–30. https://doi.org/10.1016/S1387-1811(00)00216-X.
[57] Lu J, Gao L, Sun J, Gui L, Guo J. Effect of nickel content on the sintering behavior, mechanical and dielectric properties of Al2O3/Ni composites from coated powders. Mater Sci Eng, A 2000;293(1–2):223–8. https://doi.org/10.1016/S0921-5093(00)01231-4.
[58] Xu Y, Li Y, Yang J, Sang S, Wang Q. Fabrication of MgO-NiO-Fe2O3 materials and their corrosion in Na3AlF6-AlF3-K3AlF6 bath. J Alloys Compd 2017;723:64–9. https://doi.org/10.1016/j.jallcom.2017.06.284.
[59] Liu J, Lv X, Li J, Zhang L, Peng J. Hot corrosion behavior of two-step sintered magnesium aluminate spinels in molten electrolyte. J Alloys Compd 2017;725:1313–9. https://doi.org/10.1016/j.jallcom.2017.07.287.
[60] Nickel KG, Seipel B. Corrosion penetration monitoring of advanced ceramics in hot aqueous fluids. Mater Res 2004;7:125–33. https://doi.org/10.1590/S1516-14392004000100017.
[61] Kaveh M, Mesgari MS. Application of meta-heuristic algorithms for training neural networks and deep learning architectures: a comprehensive review. Neural Process Lett 2023;55(4):4519–622. https://doi.org/10.1007/s11063-022-11055-6.
[62] Wang Y, Su F, Guo Y, Yang H, Ye Z, Wang L. Predicting the microbiologically induced concrete corrosion in sewer based on XGBoost algorithm. Case Stud Constr Mater 2022;17:e01649. https://doi.org/10.1016/j.cscm.2022.e01649.
[63] Alabdullah AA, Iqbal M, Zahid M, Khan K, Amin MN, Jalal FE. Prediction of rapid chloride penetration resistance of metakaolin based high strength concrete using light GBM and XGBoost models by incorporating SHAP analysis. Construct Build Mater 2022;345:128296. https://doi.org/10.1016/j.conbuildmat.2022.128296.